Design and Implementation of a Ferrofluid-based Liquid Robot for Small-Scale Manipulation

Fanxing Kong, Jie Zhao, Hegao Cai and Yanhe Zhu

Abstract—Magnetic manipulation of miniature soft or liquid robots capable of deformation has gained increasing attention and is demonstrating great potential in small-scale applications, such as drug delivery, minimal invasive surgery, and manipulation of delicate objects. In this study, we introduce a liquid robot composed of ferrofluid that shows promise for small-scale magnetic manipulation applications. The objective of this work is to achieve more flexible manipulation capabilities of the robot. To this end, we utilize a redundant magnetic actuation system composed of five electromagnets and implement 4 degrees of freedom (4-DOF) control of the liquid robot in planar space. Based on the planar 4-DOF control, the liquid robot is able to perform various actions and implement versatile manipulation tasks, such as transporting objects, separating or assembling miniature parts, and operating customized tools. Furthermore, we suggest an automatic transportation method to enhance manipulation precision. A series of experiments are conducted to validate the effectiveness of the proposed method and the robot's capacity to accomplish diversified manipulation tasks. The proposed liquid robot indicates flexibility and provides novel solutions for small-scale untethered manipulation.

Index Terms—Soft robot materials and design, micro/nano robots, ferrofluid, liquid robot, magnetic manipulation, automatic transportation.

I. Introduction

MANIPULATION, transportation and assembly of small objects have gained widespread attention in various fields such as materials, biology and medicine [1]. To manipulate objects in unstructured environments, miniature magnetic robots have been investigated because magnetic fields can penetrate non-magnetic materials, and the untethered control mode allows them to noninvasively access narrow spaces for manipulation tasks [2]–[4]. A variety of rigid robots with specific shapes and various microgrippers have been designed to capture or transport objects, which can be applied for assembly of heterogeneous materials, pick-and-place of micro-objects for lab-on-a-chip and biological applications [5], [6].

Due to the limited motion mode of rigid robots, miniature soft robots made of shape-programmable materials [7] have been proposed in the past decade. By applying programmed magnetic field, these soft robots can be actuated to generate desired shapes, allowing them to adapt to the surroundings [8]. Moreover, soft robots with active programmable deformation have demonstrated multimodal locomotion capabilities and higher degrees of freedom, enabling them to achieve high mobility, flexible functionalities. [9]. In addition to soft robots, swarm robots also gained attention due to their remarkable environmental adaptability and multifunctionality. They can navigate through extreme intricate environments and are suitable for manipulation tasks at micro or nano scale. Furthermore, swarm robots exhibit various collective behaviors [10], [11]. By applying dynamic magnetic fields, swarm robots can exhibit multiple patterns, allowing them to perform diverse tasks.

Recently, researchers have shown an increased interest in magnetic liquid robots composed of ferrofluid, which is a colloidal suspension of magnetic nanoparticles in a carrier liquid. Ferrofluid-based liquid robots can deform significantly under a programmed magnetic field to navigate through highly constrained spaces [12]. Numerous studies have investigated the control strategies and showcased the functionality and adaptability of ferrofluid robots using diverse magnetic fields. For instance, D. Chen used a magnet and three micromotion stages to manipulate the ferrofluid to transport objects [13]. F. Kong et al. proposed a method for integrated locomotion and deformation of the ferrofluid using four electromagnets, enabling it to transport objects through active deformation [14]. X. Fan demonstrated the capabilities of reconfigurable and multifunctional ferrofluid robots by combining electromagnets with a mobile magnet [15], [16]. In addition, time-varying magnetic fields, e.g. rotating fields, oscillating fields [17]–[21], generated by Helmholtz coils, have been used to motivate the ferrofluid to roll, wobble and split. The multimodal locomotion capabilities enhance the adaptability and functionality of ferrofluid robots, enabling them to overcome obstacles, transport objects and perform other manipulation tasks. However, the potential of the

Manuscript received: June, 17, 2023; Revised August, 26, 2023; Accepted October, 20, 2023.

This paper was recommended for publication by Editor Yong-Lae Park upon evaluation of the Associate Editor and Reviewers' comments. This work was supported by the National Outstanding Youth Science Fund Project of National Natural Science Foundation of China (Grant no. 52025054).(Corresponding author: Yanhe Zhu.)

Fanxing Kong, Jie Zhao, Hegao Cai and Yanhe Zhu are with the State Key Laboratory of Robotics and Systems, Harbin Institute of Technology, Harbin, Heilongjiang 150001, China (e-mail: fxkong@stu.hit.edu.cn; jzhao@hit.edu.cn; hgcai@hope.hit.edu.cn; yhzhu@hit.edu.cn).

Digital Object Identifier (DOI): see top of this page.

IEEE Robotics and Automation Letters (RA-L) paper, presented at ICRA 2024, Yokohama, Japan. Cite as RA-L paper.

increased degrees of freedom offered by deformation has not been fully realized. Furthermore, magnetic manipulation is usually performed manually, making it difficult to ensure accuracy. Therefore, a more precise and intelligent magnetic manipulation method needs to be developed.

In this work, we propose a ferrofluid-based liquid robot and focus on achieving versatile and precise manipulation capabilities of the robot. To this end, we design a redundant electromagnetic actuation(EMA) system composed of five stationary electromagnets to accomplish planar 4-DOF control for the liquid robot, which includes 2-DOF locomotion and 2-DOF deformation as shown in Fig. 1(a). The redundancy design reduces the singularity of the system. With the 4-DOF control, the ferrofluid can perform various actions such as pushing, poking, scooping, separating and penetrating into a narrow gap, indicating great flexibility. Consequently, complex manipulation tasks such as transporting, sorting, assembling and operating customized tools can be performed. Furthermore, we present an automatic method to improve the precision of transportation, which allows the object to be transported along a desired trajectory with minor errors. Compared to previous studies, the key innovation of this paper lies in the precise cooperative control of deformation and locomotion, which enables a variety of actions and more flexible manipulation. We not only ensure the robot's movement accuracy but also achieve precise control of the manipulated object. Several experiments have been implemented to demonstrate the capabilities of the liquid robot, indicating great potential for small-scale manipulation applications.

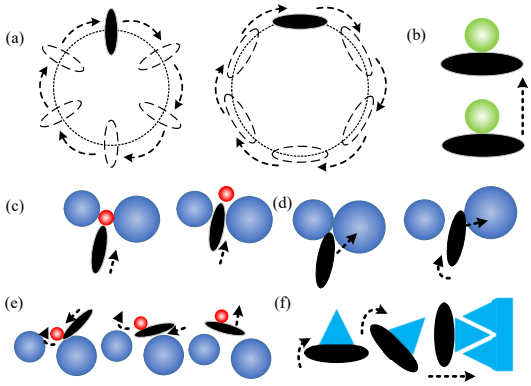

Fig. 1. Schematic diagram of the 4-DOF control and versatile actions of the ferrofluid. (a) Cooperative locomotion and deformation. (b) Pushing an object. (c) Poking a small object out of a gap. (d) Separating the objects. (e) Scooping a small ball.(f) Adjusting the attitude of the object and assembling.

II. Modeling

A. Magnetic Field

In an external magnetic field with strength $\mathbf{H}$(A/m), the ferrofluid is magnetized and the magnetic density $\mathbf{B}$(T) is

$$\mathbf{B} = \mu_0(\mathbf{H} + \mathbf{M}) = \mu_0(\mathbf{1} + \chi)\mathbf{H} \tag{1}$$

where μ_0 is the magnetic permeability of vacuum, $\mathbf{M} = \chi\mathbf{H}$ denotes the magnetization of ferrofluid and χ is the susceptibility. The ferrofluid has no hysteresis effect, and according to the magnetization curve of ferrofluid [21], the magnetization is nearly linear when $\mathbf{H}$ is small. Thus χ is considered as a constant in this case. The magnetic field $\mathbf{B} = \begin{bmatrix} B_x & B_y \end{bmatrix}^T$ at a position $\mathbf{P} = \begin{bmatrix} x & y \end{bmatrix}^T$ generated by the proposed magnetic actuation system can be written as

$$\begin{bmatrix} B_x \\ B_y \end{bmatrix} = \begin{bmatrix} B_{1x} & B_{2x} & \dots & B_{5x} \\ B_{1y} & B_{2y} & \dots & B_{5y} \end{bmatrix} \mathbf{I} = \begin{bmatrix} \mathbf{B_{sx}} \\ \mathbf{B_{sy}} \end{bmatrix} \mathbf{I} \tag{2}$$

where $\mathbf{B_{sx}}$, $\mathbf{B_{sy}} \in \mathbb{R}^{1\times5}$, B_{ix} and B_{iy} are the magnetic intensity components generated by a unit current of the i_{th} electromagnet at position $\mathbf{P}$. $\mathbf{I} \in \mathbb{R}^5$ is the current of the electromagnets. The gradient of the magnetic field is

$$\begin{bmatrix} \frac{\partial B_x}{\partial x} \\ \frac{\partial B_x}{\partial y} \\ \frac{\partial B_y}{\partial x} \\ \frac{\partial B_y}{\partial y} \end{bmatrix} = \begin{bmatrix} \frac{\partial B_{x1}}{\partial x} & \frac{\partial B_{x2}}{\partial x} & \dots & \frac{\partial B_{x5}}{\partial x} \\ \frac{\partial B_{x1}}{\partial y} & \frac{\partial B_{x2}}{\partial y} & \dots & \frac{\partial B_{x5}}{\partial y} \\ \frac{\partial B_{y1}}{\partial x} & \frac{\partial B_{y2}}{\partial x} & \dots & \frac{\partial B_{y5}}{\partial x} \\ \frac{\partial B_{y1}}{\partial y} & \frac{\partial B_{y2}}{\partial y} & \dots & \frac{\partial B_{y5}}{\partial y} \end{bmatrix} \mathbf{I} = \begin{bmatrix} \mathbf{B_{xx}} \\ \mathbf{B_{xy}} \\ \mathbf{B_{yx}} \\ \mathbf{B_{yy}} \end{bmatrix} \mathbf{I} \tag{3}$$

where $\mathbf{B_{xx}}$, $\mathbf{B_{xy}}$, $\mathbf{B_{yx}}$, $\mathbf{B_{yy}} \in \mathbb{R}^{1\times5}$, $\frac{\partial B_{xi}}{\partial x}$, $\frac{\partial B_{xi}}{\partial y}$, $\frac{\partial B_{yi}}{\partial x}$ and $\frac{\partial B_{yi}}{\partial y}$ are the gradient components generated by a unit current of the i_{th} electromagnet at position $\mathbf{P}$.

B. Magnetic Force

In a gradient magnetic field, the macroscopic total magnetic force $\mathbf{F_{mag}}$ exerted on the ferrofluid is [22]

$$\mathbf{F_{mag}} = V(\mathbf{M} \cdot \nabla)\mathbf{B} \tag{4}$$

where V denotes the volume of the ferrofluid droplet. Substitute (1), (2) and (3) into (4), $\mathbf{F_{mag}}$ is simplified as

$$\mathbf{F_{mag}} = \begin{bmatrix} F_x & F_y \end{bmatrix}^T = \begin{bmatrix} k\mathbf{B}^T\mathbf{R}\mathbf{I} & k\mathbf{B}^T\mathbf{S}\mathbf{I} \end{bmatrix}^T \tag{5}$$

where $k = \frac{V\chi}{\mu_0(1+\chi)}$ is the coefficient, F_x and F_y are the components of $\mathbf{F_{mag}}$, $\mathbf{R}$ and $\mathbf{S}$ are the magnetic gradient matrixes

$$\mathbf{R} = \begin{bmatrix} \mathbf{B_{xx}} \\ \mathbf{B_{xy}} \end{bmatrix}, \mathbf{S} = \begin{bmatrix} \mathbf{B_{yx}} \\ \mathbf{B_{yy}} \end{bmatrix} \tag{6}$$

Therefore, the magnetic force $\mathbf{F_{mag}}$ is related to both the field intensity and gradient. Since magnetic field $\mathbf{B}$ is proportional to coil current $\mathbf{I}$ [14], $\mathbf{F_{mag}}$ is actually the quadratic form of $\mathbf{I}$.

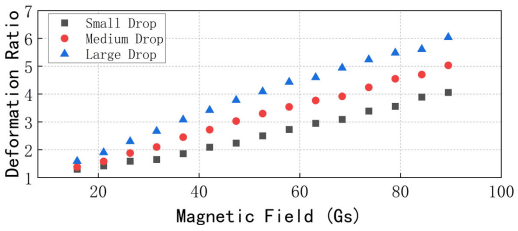

Fig. 2. Deformation of the ferrofluid of different volumes.

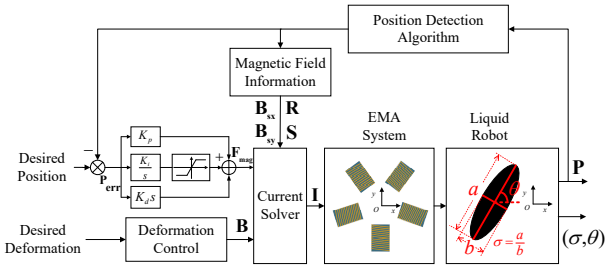

Fig. 3. Schematic diagram of the 4-DOF control.

C. Kinetics Model

The robot is manipulated in water environment in a petri dish and the friction between the ferrofluid and the container is neglected due to the buoyancy force. Only the magnetic force $\mathbf{F_{mag}}$ and viscous drag force are taken into account. The viscous drag force is proportional to the motion speed $\mathbf{v}$

$$\mathbf{f_d} = k_d \mathbf{v} \tag{7}$$

where k_d is a constant related to the radius of the ferrofluid and the viscosity coefficient. So the kinetics model is

$$\mathbf{F_{mag}} - k_d \mathbf{v} = m \frac{d^2 \mathbf{P}}{dt^2} \tag{8}$$

where m denotes the mass of ferrofluid.

III. METHOD

A. 4-DOF Control

Deformation of the ferrofluid involves two degrees of freedom: the magnitude and the direction, represented by the deformation ratio σ and deformation angle θ, respectively. σ is defined as the aspect ratio $\frac{a}{b}$, where a and b denote the length and width of the ferrofluid. In a magnetic field, the deformation results from the combined effect of magnetic force and surface tension. The ratio between magnetic force and surface tension is denoted as $B_{Om} = \frac{\mu_0 \chi V^{\frac{1}{3}} H^2}{2\tau}$, where τ denotes the surface tension coefficient [23]. Higher B_{Om} leads to a further stretching of the droplet. Therefore, the deformation is influenced by both the magnetic field strength and the size. The deformation of ferrofluid with different volumes is measured under various magnetic fields, as illustrated in Fig. 2. It is evident that higher field intensity leads to larger deformation. Meanwhile, with the same magnetic field conditions, larger volumes of ferrofluid exhibit more pronounced deformation, signifying a more distinct fluidic behavior. Conversely, smaller droplets exhibit less fluidic characteristics. To achieve the same deformation ratio, smaller volume droplets require a larger magnetic field.

Deformation angle is defined as the angle between the long axis of the ferrofluid and the x-axis of the fixed coordinate system. In a slowly changing magnetic field, the deformation direction of the robot aligns with the magnetic field direction. Thus, the relationship between the ferrofluid's deformation and the magnetic field $\mathbf{B}$ can be expressed as

$$\begin{cases} \sigma \propto |\mathbf{B}| = \sqrt{B_x^2 + B_y^2} \\ \theta = \arg \mathbf{B} = \arcsin \dfrac{B_y}{\sqrt{B_x + B_y}} \end{cases} \tag{9}$$

By selecting suitable values for σ and θ, and applying corresponding $|\mathbf{B}|$ and $\arg \mathbf{B}$, the ferrofluid can achieve the desired deformation. When both $|\mathbf{B}|$ and $\arg \mathbf{B}$ remain constant, the ferrofluid exhibits static deformation. In the case where $|\mathbf{B}|$ varies with time while $\arg \mathbf{B}$ remains fixed, the ferrofluid undergoes continuous stretching and contracting. On the other hand, when $|\mathbf{B}|$ is constant and $\arg \mathbf{B}$ varies with time, the ferrofluid undergoes rotational motion.

The planar locomotion of the ferrofluid is achieved by controlling the magnetic force $\mathbf{F_{mag}}$. By considering $\mathbf{F_{mag}}$ as the system input, equation (9) can be transformed into a standard second-order linear system. A PID controller with integral windup limitation is adopted to achieve closed-loop control. Combining (2) and (5), we obtain a system of linear equations [22]

$$\begin{bmatrix} \mathbf{F_{mag}}(\mathbf{P_{err}}) \\ \mathbf{B}(\sigma, \theta) \end{bmatrix} = \begin{bmatrix} k\mathbf{B}^T\mathbf{R} \\ k\mathbf{B}^T\mathbf{S} \\ \mathbf{B_{sx}} \\ \mathbf{B_{sy}} \end{bmatrix} \mathbf{I} = \mathbf{G}\mathbf{I} \tag{10}$$

where $\mathbf{F_{mag}}$ is a function of the position error $\mathbf{P_{err}}$, and $\mathbf{B}$ is determined by the desired deformation ratio σ and deformation angle θ. $\mathbf{G} \in \mathbb{R}^{4\times5}$ represents the magnetic field information, incorporating known system parameters such as $\mathbf{R}$, $\mathbf{S}$, $\mathbf{B_{sx}}$ and $\mathbf{B_{sy}}$. By generating an appropriate magnetic force $\mathbf{F_{mag}}$ under a specific magnetic field $\mathbf{B}$, and solving (15), the required currents for cooperative locomotion and deformation are obtained

$$\mathbf{I} = \mathbf{G}^{\dagger} \begin{bmatrix} \mathbf{F_{mag}}(\mathbf{P_{err}}) \\ \mathbf{B}(\sigma, \theta) \end{bmatrix} \tag{11}$$

where $\mathbf{G}^{\dagger}$ is the pseudo inverse of $\mathbf{G}$. The schematic diagram of the 4-DOF control is shown in Fig. 3.

Through different combinations of deformation and locomotion, the ferrofluid exhibits versatile actions and can performs various tasks. As depicted in Fig. 1, when the motion direction is perpendicular to the deformation direction, the ferrofluid can transport objects. When the motion

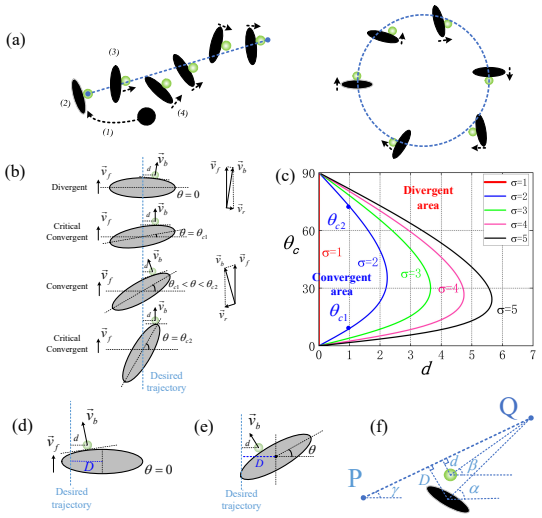

Fig. 4. (a) Schematic diagram of the automatic transportation. (b) Adjusting the ball by alternating the deformation angle. (c) Relationship between critical convergence deformation angle $theta_c$ and offset distance d. (d) Adjusting the ball by applying a lateral displacement D. (e) Adjusting the ball by alternating deformation angle and applying a lateral displacement. (f) Definition of the geometric relations in the case of straight line transportation.

direction aligns with the deformation direction, the ferrofluid can penetrate narrow gaps and execute poking actions, making it suitable for manipulating objects in confined spaces. When the motion direction forms an acute angle with the deformation direction, the ferrofluid can separate adjacent objects and push them aside. By rotating the deformation angle, the ferrofluid can adjust the orientation of the object or stir liquids. Additionally, when the ferrofluid penetrate into a gap and undergoes a specific rotation, it can execute scooping actions and then move the object away.

B. Automatic Transportation

An automatic transportation strategy is proposed which allows the ferrofluid to autonomously transport objects along desired trajectories, indicating a high manipulation precision. The schematic diagram of automatic transportation is illustrated in Fig. 4(a). The ferrofluid can adjust the position of a ball by altering the deformation angle θ and applying a lateral displacement D. In the straight line transportation, if the small ball deviates from the desired trajectory by a distance d, the ferrofluid's deformation angle determines the motion trend of the small ball. This principle is illustrated in Fig. 4(b) through velocity decomposition: $\overrightarrow{v_b} = \overrightarrow{v_f} + \overrightarrow{v_r}$, where $\overrightarrow{v_b}$ is the ball's velocity, $\overrightarrow{v_f}$ is the ferrofluid's velocity, and $\overrightarrow{v_r}$ is the relative velocity between the ball and the ferrofluid. When $\theta = 0$, due to curvature, the ball will continue to deviate from the trajectory along the ferrofluid's surface. When θ equals θ_{c1} or θ_{c2}, the force exerted on the ball is parallel to the trajectory, indicating a critical convergence state. When $\theta_{c1} < \theta < \theta_{c2}$, the ball will converge back towards the trajectory. The deformed ferrofluid can be geometrically understood as an ellipse. By analyzing the geometric relationships (See the Appendix), we can derive the relationship between the offset distance d and the critical convergent deformation angle θ_c

$$d = \frac{a^2 - b^2}{\sqrt{1 + \frac{1}{\tan^2\theta_c}}\sqrt{a^2\tan^2\theta_c + b^2}} \tag{12}$$

The θ_c-d curve at different σ is plotted in Fig. 4(c). When σ is 1, the ferrofluid is a circular shape, which is impossible to push the ball back to the trajectory through rotation. When d is 1 and the σ is 2, a pair of θ_{c1} and θ_{c2} values can be determined. Within the range of $\theta_{c1} < \theta < \theta_{c2}$, the transportation is convergent. The region enclosed by the curve and the y-axis denotes the range of convergent deformation angles. Evidently, a higher σ results in a broader convergent region. However, for a fixed σ, the ball converges only within a specific range of d. If d becomes too large, the ferrofluid cannot push the ball back to the trajectory through rotation. In such instances, convergence can be achieved by either increasing σ or implementing lateral movement D. As portrayed in Fig. 4(d), when $D > d$, the ferrofluid can push the ball back. Based on above analysis, we can formulate an automatic strategy for straight line transportation. When $d = 0$, the ferrofluid propels the small ball along the trajectory. When d is small, the ferrofluid rotates a certain angle to push the ball back to the trajectory. When d is large, the ferrofluid moves laterally by a distance D and rotates by a certain angle to bring the small ball back to the trajectory.

The geometric relations of the straight line transportation is depicted in Fig. 4(f). The initial position is $\mathbf{P}$ and the target position is $\mathbf{Q}$. The goal is to transport the ball from $\mathbf{P}$ to $\mathbf{Q}$ along the straight line $\overrightarrow{\mathbf{PQ}}$. Assuming the azimuth angle of the straight line $\overrightarrow{\mathbf{PQ}}$ is γ, the azimuth angle of the ferrofluid is α, the azimuth angle of the ball is β. α, β, γ and d can all be obtained from visual feedback, θ and D are functions of α, β, γ and d, that is, $[\theta, D] = f(\alpha, \beta, \gamma, d)$. The operation rules of function f were determined through multiple experiments, following the abovementioned automatic transportation strategy.

The entire automatic transportation process is realized using a state machine. Firstly, initialize the task and obtain information through visual feedback. Then it enters into State A. In State A, the ferrofluid gradually approaches the object and moves behind it. When the ferrofluid is close enough to the object, it transitions to State B. In State B, the required θ and D are determined based on the rule $[\theta, D] = f(\alpha, \beta, \gamma, d)$. The corresponding deformation and lateral movement are subsequently executed, leading to State C. In State C, the ferrofluid moves one step to propel the ball forward, after which it reverts back to State B and the process is repeated. Throughout the entire process, the

distance between the ferrofluid and the manipulated object is detected in real-time. If the manipulated object becomes detached from the ferrofluid, the system transitions to State A, and the corresponding actions of State A are re-executed.

Transportation on a circular or curved trajectory is similar to that on a straight line trajectory, except that the azimuth angle γ of the straight trajectory is replaced by the azimuth angle of the tangent line.

IV. EXPERIMENTS

A. Experimental Setup

The experiments were conducted on the EMA system consisting of five electromagnets arranged in a planar configuration at 72-degree intervals, shown in Fig. 5(a). The resistance of each coil is 8Ω, and each electromagnet is powered by a 20-volt DC supply, allowing a maximum coil current of 2.5A and a maximum power of 50W. At a current of 2.5A, one electromagnet can generate a field of 150mT near the iron core, and 6.5mT at the center of the workspace, with a magnetic field gradient of about 0.2T/m. The field data of a single electromagnet was measured on a plane and fitted into a surface, as shown in Fig. 5(b) and Fig. 5(c). A camera captures images at a rate of 50 fps to detect the positions of the ferrofluid and the manipulated object, as well as the deformation angle and aspect ratio. The experimental range of motion for the ferrofluid is approximately a rectangular area of 56mm by 42mm. The camera has a resolution of 512 by 384 pixels, resulting in a visual feedback accuracy of about 0.11mm. Visual feedback algorithms and control algorithms were developed using OpenCV and C++ with a running cycle of 20ms. Current commands for the coils are calculated by the controller and then transmitted to a DSP to generate PWM signals. Then the DC motor drivers propel the electromagnets to produce the required magnetic field. The ferrofluid is bought by Taobao. In the experiments, the droplet has a volume of about 0.02ml and is placed in a petri dish with a diameter of 70mm filled with water. The viscosity is 20cp at a temperature of 25 degrees. It reaches saturated magnetization when the field is 0.045T and the initial magnetic susceptibility is 0.8.

B. 4-DOF Control

The ferrofluid was actuated to move along a circular trajectory with a diameter of 26.4 mm and a frequency of 0.2 rad/s or 0.4 rad/s, exhibiting non-deformation, radial deformation, and tangential deformation modes. The average velocity is about 2.6mm/s. The length of the ferrofluid remained constant by maintaining a constant magnetic field magnitude, while the deformation angle was controlled by varying the direction of the magnetic field. Fig. 6 illustrates the experimental results and the corresponding time-lapse image sequences. The results show that in radial or tangential deformation mode, the ferrofluid moved along the

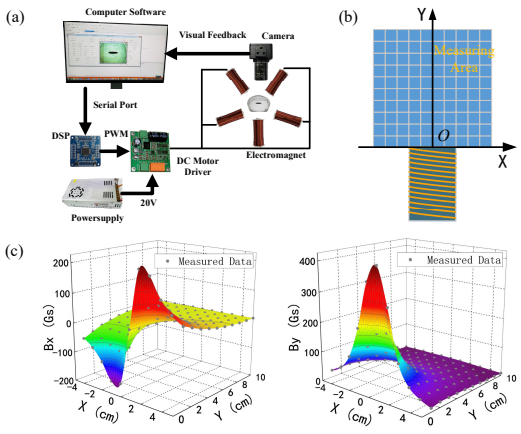

Fig. 5. (a)Experimental setup. (b) Schematic diagram of magnetic field measurement of a single electromagnet. The field is measured on a 10cm by 10cm grid plane. (c) Discrete measurement values and fitted surfaces.

circle path while the deformation angle was continuously adjusted to maintain its orientation towards the center or tangent to the circle. In the non-deformation mode, the position errors were generally within 0.6 mm. In the radial or tangential deformation mode, the errors were larger than those without deformation, with errors typically in the range of 0.9 mm. However, the errors were still within acceptable limits. Compared with the previous research [24], our robot demonstrates a larger range of motion and lower relative error. There are some reasons for the increased tracking error caused by deformation. First, the deformation changes the hydrodynamic dynamics, where water resistance is no longer a simple damping factor. The alteration in hydrodynamic model due to deformation requires further research. Secondly, the ferrofluid's magnetization increased with the deformation. In the model, magnetization is treated linearly by assuming the magnetization coefficient χ to be constant. However, the ferrofluid's magnetization is nonlinear. As deformation increases, the magnetization coefficient varies, introducing higher uncertainty into the model. Furthermore, in the magnetic field model, undeformed ferrofluid can be treated as a point mass. Only the magnetic field at the center of the ferrofluid were considered. However, as the ferrofluid is stretched, it can no longer be treated as a point mass. The magnetic field at the edges of the ferrofluid differs from that at the center, leading to variations in the overall magnetic force it experiences.

C. Versatile Actions and Manipulations

A series of manipulation experiments were conducted based on the 4-DOF control to assess the ferrofluid's ability to perform various actions and accomplish diversified manipulation tasks. Fig.7 (a) illustrates the ability of operating miniature tools through cooperative locomotion and deformation. A 3D-printed miniature shovel is manipulated by the ferrofluid to

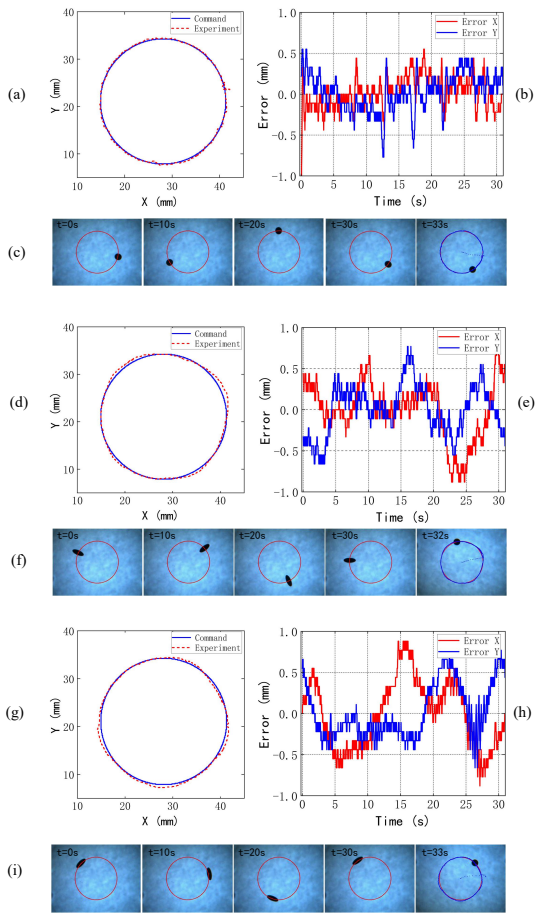

Fig. 6. Experiments of the 4-DOF control in which the ferrofluid moves along a circle trajectory in the modes of non-deformation, radial deformation and tangential deformation respectively. The diameter is 26.4mm and the frequency is 0.2rad/s. (a)-(c) Trajectory of the ferrofluid, errors on the X and Y axes, and time image sequences of non-deformation mode. (d)-(f) Trajectory of the ferrofluid, errors on the X and Y axes, and time image sequences of radial deformation mode. The deformation keeps pointing to the center of the circle. (g)-(h) Trajectory of the ferrofluid, errors on the X and Y axes, and time image sequences of tangential deformation mode. The deformation angle keeps tangent to the circle.

transport objects. The ferrofluid can simultaneously adjust the position and attitude of the shovel by moving, deforming and rotating, enabling easy pushing of multiple objects. This tool manipulation ability enhances the versatility of the liquid robot, enabling customization of various tool types for complex task handling. It can also be utilized for precise assembly of different components, as depicted in Fig. 7(b). In Fig. 7(c), the ferrofluid is employed to assemble multiple objects into a specific shape. Initially, several triangle objects are randomly placed. Then the ferrofluid sequentially transports each triangle to its designed position, adjusting their orientation through rotation, and eventually making them fit together as a whole. Ultimately, the ferrofluid utilizes increased deformation to move the entire structure. In addition to pushing, the ferrofluid can perform poking and scooping actions, as demonstrated in Fig. 7(d) and Fig. 7(e). It can use its tip to poke small objects in narrow spaces, penetrate gaps, and scoop objects. Furthermore, comprehensive manipulation experiments were conducted, showcasing the ferrofluid's ability to separate, sort, and transport objects, as shown in Fig. 7(f) and Fig. 7(g). Initially, objects of different sizes and colors are placed closely together. The ferrofluid stretches and inserts itself into gaps, separates nearby objects by rotating, or pushes an object out of gap by poking with its tip. Through a series of operations, the ferrofluid arranges objects neatly based on their size and color. Subsequently, the ferrofluid separates each object gently using its tip and divides them into three piles. These experiments indicate that the 4-DOF locomotion enhances the robot's flexibility, enabling it to perform a variety of manipulation tasks.

D. Automatic Transportation

The manipulation experiments mentioned above are performed manually, which is difficult to guarantee the accuracy and effectiveness when dealing with some precision tasks. To demonstrate the ability of precise manipulation of the liquid robot, automatic transportation experiments are carried out. In these experiments, the ferrofluid automatically propels a small ball along a predetermined straight or circular trajectory. The experimental process of automatic transportation is shown in Fig. 8. Initially, the ferrofluid automatically approaches and moves behind the small ball, deforms, and then pushes the small ball forward along the straight line direction or the tangent direction of the circle. When the ball deviates from the trajectory, the ferrofluid automatically adjusts its position and attitude, so as to make the small ball return to the trajectory. The position data and trajectory in Fig. 8(a) and Fig. 8(b) demonstrate that the ball moves approximately 20mm from t=13s to t=31s, along an actual trajectory that is roughly a straight line. The position error typically remains within 0.6mm. Fig. 8(d) and Fig. 8(e) illustrate the circular automatic transportation. The ball travels two circles in 75 seconds at an average speed of 2.1mm/s. The actual trajectory is close to the desired circular path, whose diameter is 25mm, and the error typically remains within 1mm. These experiments not only ensure precise motion of the robot, but also achieve high precision in manipulating the object. The experimental results indicate potential in small-scale precision manipulation.

E. Discussion

There are various methods for manipulating micro-scale objects using robots. One approach involves attaching the target objects onto the robot's surface. By designing specific shapes and structures, such as porous structure [25], objects such as cells can adhere to the robot and be transported to the desired position. J. Li et al. devised a burr-like

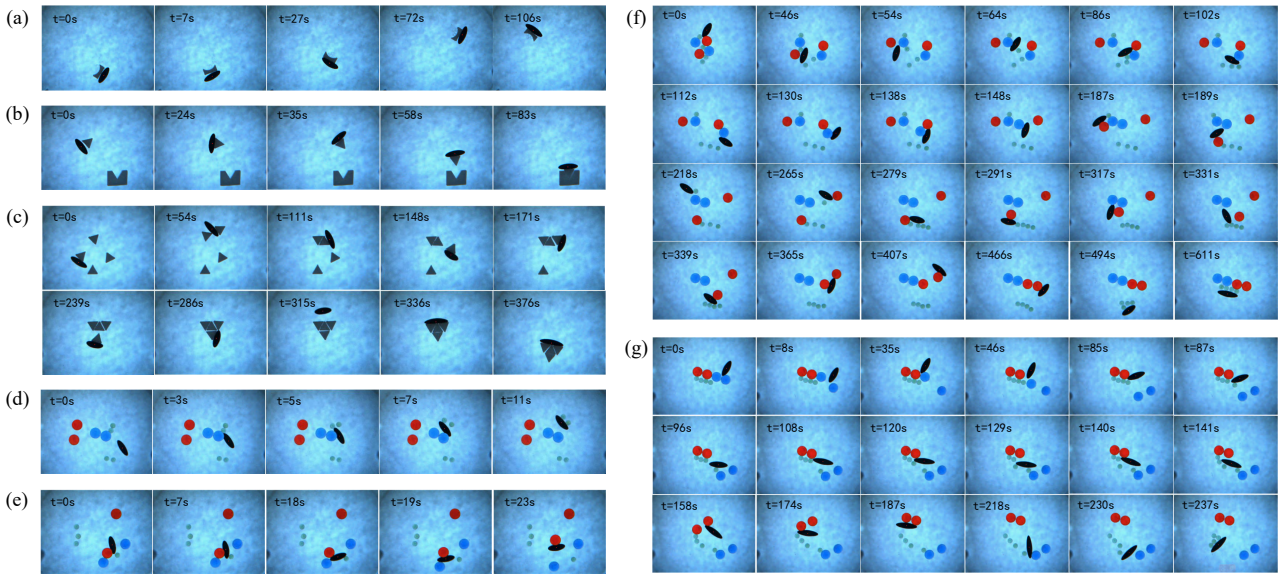

Fig. 7. Experimental demonstration of versatile actions and manipulation tasks. (a) The ferrofluid operates a customized miniature shovel tool to transport multiple small balls. (b) The ferrofluid adjusts the position and attitude of a triangular part to fit it to another part. (c) The ferrofluid manipulates multiple triangles, putting them together to form a whole and pushing the whole forward. (d) The ferrofluid pokes a small ball using its tip. (e) The ferrofluid scoops a red ball. (f) The ferrofluid sorts and arranges cluttered objects neatly. (g) The ferrofluid separates the objects gently and sorts them into three piles.

porous spherical structure driven by 6 electromagnetic coils to carry cells at a speed of 1mm/s [26]. The maximum coil current is 10A and the response speed is 30 ms. However, this method has limited functionality, primarily suitable for object transport. Micro grippers are a commonly choice for tasks like grasping, transporting, and releasing objects. E. Diller devised a gripper actuated by 8 coils that can grasp and manipulate objects with sub-millimeter precision. This robot successfully assembled 3D four-bar linkage within 90 minutes [27]. F. Ongaro developed a hexagram-shaped gripper with the size of 4 mm. This gripper achieves pick-and-place tasks involving biological material at an average velocity of 1.80 ± 0.71 mm/s and a error of 0.62 ± 0.22 mm [28]. Furthermore, S. Tottori developed a helical micromachine embedding a microholder for object confinement and transportation. This micromachine achieves speeds ranging from approximately 0.02 mm/s to 0.18 mm/s [29]. S. Tasoglu et al. proposed a method for both 2D and 3D material composition. This robot is propelled by 8 electromagnetic coils, with a maximum current of 19A per coil. It completed 2D material assembly in 17 minutes and constructed a three-layer heterogeneous pyramid structure in 26 minutes [1].

The proposed liquid robot operates mainly at the millimeter scale, achieving speeds of 2.1mm/s, with precise object positioning within a 1mm range. The maximum current for the electromagnetic coil is 2.5A. During manipulation tasks, the coil currents remain within 1.5A, resulting in a total power consumption of around 30W. Compared to other manipulation robots, the magnetic fluid robot offers high flexibility and accuracy in manipulating objects, and is capable of performing various actions. Its soft contact surface makes it suitable for handling extremely fragile objects. However, there are still untapped potentials in ferrofluid robots, such as harnessing its deformation, splitting, merging, and engulfing abilities to achieve more diversified operations in complex 3D spaces, which is both promising and challenging. Additionally, considering the impact of size on deformation capability, controlling magnetic fluid operations at the micrometer scale also requires further research.

V. CONCLUSION AND FUTURE WORK

A liquid robot composed of ferrofluid has been proposed in this work, showcasing its promising ability and flexibility in small-scale manipulation applications. Based on the planar 4-DOF control under a redundant magnetic actuation system, various actions of the robot were implemented for different manipulation tasks and an automatic transportation strategy was proposed to improve the manipulation precision. A series of experiments were carried out to validate the effectiveness of the proposed control method and the robot's ability to accomplish diversified manipulation tasks. The ferrofluid was found to be capable of performing a variety of actions such as pushing, poking, scooping, exhibiting considerable flexibility and enabling the robot to handle more complex tasks. Furthermore, precise transportation were accomplished. The motion error of the robot generally remained within a range of 0.9 mm, and the error of the manipulated object was within 1 mm. In future work, we will consider planning

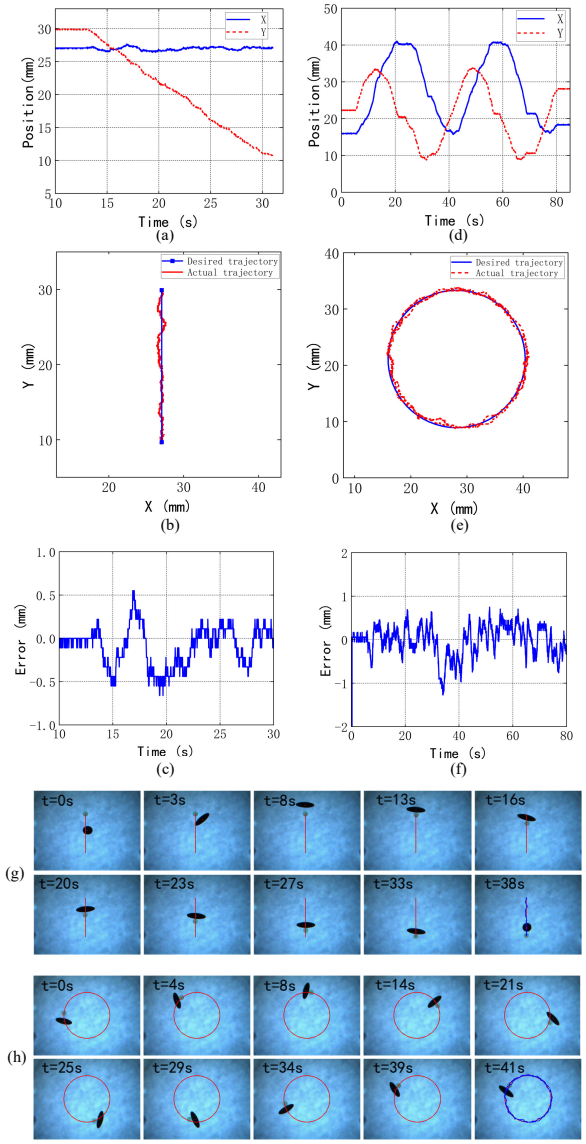

Fig. 8. Automatic transportation experiments. The ferrofluid automatically pushes a small ball along the desired straight or circular trajectory. (a) Movement of the ball along the straight line. (b) Actual trajectory of the ball in straight automatic transportation. (c) Error of the ball in straight transportation. (d) Movement of the ball along the circle. (e) Actual trajectory of the ball in circular automatic transportation.(f) Error of the ball in circular transportation. (g) Time image sequences in straight automatic transportation. (h)Time image sequences in circular automatic transportation.

tasks and trajectories in 3D environments to enable the robot to complete manipulation tasks more autonomously and intelligently.

Appendix

When the ball deviates from the trajectory by a distance of d and the ferrofluid propels the ball with the angle $\theta = \theta_c$, the velocity of the ball is parallel to the trajectory, that

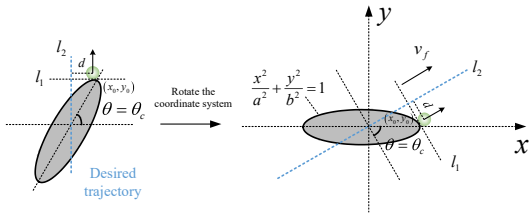

Fig. 9. Geometrical relationship at critical convergence state.

is, the critical convergence state illustrated in Fig. 9. The ferrofluid can be considered as an ellipse, with a major axis of a and a minor axis of b. The tangent line at the contact point $\mathbf{M}(x_0, y_0)$ is $\vec{l1}$, and $\vec{l1} \perp \vec{l2}$. The distance between $\mathbf{M}$ and $\vec{l2}$ is d. Rotate the coordinate system and the ellipse representing the ferrofluid is $\frac{x^2}{a^2} + \frac{y^2}{b^2} = 1$. $\mathbf{M}(x_0, y_0)$ is on the ellipse, so $\frac{{x_0}^2}{a^2} + \frac{{y_0}^2}{b^2} = 1$. The tangent line $\vec{l1}$ at $\mathbf{M}$ is $\frac{x_0}{a^2}x + \frac{y_0}{b^2}y = 1$, and the slope of line $\vec{l1}$ is

$$k = -\frac{b^2 x_0}{a^2 y_0} = \tan(\pi - \theta_c) = -\tan\theta_c \tag{13}$$

Then we obtain

$$y_0 = \frac{b^2}{\sqrt{b^2 + a^2 \tan^2\theta}} \tag{14}$$

Since $\vec{l1} \perp \vec{l2}$, the equation of line $\vec{l2}$ is $\frac{1}{\tan\theta_c}x - y = 0$. Then the distance from point $\mathbf{M}$ to line $\vec{l2}$ can be derived as

$$d = \frac{\frac{x_0}{\tan\theta_c} - y_0}{\sqrt{\frac{1}{\tan^2\theta_c} + 1}} \tag{15}$$

Substitue (14) into (15), the relationship between θ_c and d is

$$d = \frac{a^2 - b^2}{\sqrt{1 + \frac{1}{\tan^2\theta_c}}\sqrt{a^2\tan^2\theta_c + b^2}} \tag{16}$$

References

[1] S. Tasoglu, E. Diller, S. Guven, M. Sitti and U. Demirci, "Untethered micro-robotic coding of three-dimensional material composition," Nat. Commun., vol. 5, no. 3124, pp. 61¨C70, 2014.
[2] Q. Cao, Q. Fan, Q. Chen, C. Liu, X. Han and L. Li, "Recent advances in manipulation of micro- and nano-objects with magnetic fields at small scales," Mater. Horizons., vol. 7, no. 3, pp. 638–666, 2020.
[3] H. Zhou, C. C. Mayorga-Martinez, S. Pan¨¦, L. Zhang and M. Pumera, "Magnetically Driven Micro and Nanorobots," Chem. Rev., vol. 121, no. 8, pp. 4999–5041, 2021.
[4] M. Koleoso, X. Feng, Y. Xue, Q. Li, T. Munshi and X. Chen, "Micro/nanoscale magnetic robots for biomedical applications," Mater. Today Bio., vol. 8, p. 100085, 2020.
[5] T. Y. Huang et al., "Cooperative manipulation and transport of microobjects using multiple helical microcarriers," RSC Adv., vol. 4, no. 51, pp. 26771–26776, 2014.
[6] J. Zhang, O. Onaizah, K. Middleton, L. You and E. Diller, "Reliable Grasping of Three-Dimensional Untethered Mobile Magnetic Microgripper for Autonomous Pick-and-Place," IEEE Robot. Autom. Lett., vol. 2, no. 2, pp. 835–840, 2017.

[7] G. Z. Lum et al., "Shape-programmable magnetic soft matter," Proc. Natl. Acad. Sci., vol. 113, no. 41, pp. E6007–E6015, 2016.
[8] M. Sitti, "Miniature soft robots - road to the clinic," Nat. Rev. Mater., vol. 3, no. 6, pp. 74–75, 2018.
[9] W. Hu, G. Z. Lum, M. Mastrangeli and M. Sitti, "Small-scale soft-bodied robot with multimodal locomotion," Nature, vol. 554, no. 7690, pp. 81–85, 2018.
[10] L. Yang and L. Zhang, "Motion Control in Magnetic Microrobotics: From Individual and Multiple Robots to Swarms," Annu. Rev. Control. Robot. Auton. Syst., vol. 4, pp. 509¨C534, 2021.
[11] J. Yu, T. Xu, Z. Lu, C. I. Vong, and L. Zhang, "On-Demand Disassembly of Paramagnetic Nanoparticle Chains for Microrobotic Cargo Delivery," IEEE Trans. Robot., vol. 33, no. 5, pp. 1213–1225, 2017.
[12] X. Zhang, L. Sun, Y. Yu and Y. Zhao, "Flexible Ferrofluids: Design and Applications," Adv. Mater., vol. 31, no. 51, pp. 1–35, 2019.
[13] D. Chen, Z. Yang, Y. Ji, Y. Dai, L. Feng, and F. Arai, "Deformable ferrofluid-based millirobot with high motion accuracy and high output force," Appl. Phys. Lett., vol. 118, no. 13, 2021.
[14] F. Kong, Y. Zhu, C. Yang, H. Jin, J. Zhao and H. Cai, "Integrated Locomotion and Deformation of a Magnetic Soft Robot: Modeling, Control, and Experiments," IEEE Trans. Ind. Electron., vol. 68, no. 6, pp. 5078–5087, 2020.
[15] X. Fan, X. Dong, A. C. Karacakol, H. Xie and M. Sitti, "Reconfigurable multifunctional ferrofluid droplet robots," Proc. Natl. Acad. Sci., vol. 117, no. 45, pp. 27916–27926, 2020.
[16] X. Fan et al., "Scale-reconfigurable miniature ferrofluidic robots for negotiating sharply variable spaces," Sci. Adv., vol. 8, no. 37, p. eabq1677, 2022.
[17] X. Fan, M. Sun, L. Sun and H. Xie, "Ferrofluid Droplets as Liquid Microrobots with Multiple Deformabilities," Adv. Funct. Mater., vol. 30, no. 24, pp. 1–12, 2020.
[18] L. Yang, M. Sun and L. Zhang, "Torque-Actuated Multimodal Locomotion of Ferrofluid Robot With Environment and Task Adaptability," in 2022 IEEE/RSJ International Conference on Intelligent Robots and Systems (IROS), Kyoto, Japan, 2022, pp. 2542–2547.
[19] L. Yang, M. Sun, M. Zhang and L. Zhang, "Multimodal Motion Control of Soft Ferrofluid Robot With Environment and Task Adaptability," IEEE/ASME Trans Mechatron, vol. 28, no. 6, pp. 3099–3109, 2023.
[20] M. Sun, B. Hao, S. Yang, X. Wang, C. Majidi and L. Zhang, "Exploiting ferrofluidic wetting for miniature soft machines," Nat. Commun., vol. 13, no. 1, pp. 1–15, 2022.
[21] M. A. Bijarchi, A. Favakeh, E. Sedighi and M. B. Shafii, "Ferrofluid droplet manipulation using an adjustable alternating magnetic field," Sensors Actuators, A Phys., vol. 301, p. 111753, 2020.
[22] B. E. Kratochvil, M. P. Kummer, J. J. Abbott, R. Borer, O. Ergeneman and B. J. Nelson, "OctoMag: An Electromagnetic System for 5-DOF Wireless Micromanipulation," IEEE Trans. Robot., vol. 26, no. 6, pp. 1080–1081, 2010.
[23] G. P. Zhu, N. T. Nguyen, R. V. Ramanujan and X. Y. Huang, "Nonlinear Deformation of a Ferrofluid Droplet in a Uniform Magnetic Field," Langmuir, vol. 27, no. 24, pp. 14834–14841, 2011.
[24] R. Ahmed et al., "A Shapeshifting Ferrofluidic Robot," Soft Robotics., vol. 8, no. 6, pp. 687–698, 2021.
[25] S. Jeon et al., "Magnetically actuated microrobots as a platform for stem cell transplantation," Sci. Robot., vol. 4, no. 30, pp. 1–12, 2019.
[26] J. Li et al., "Development of a magnetic microrobot for carrying and delivering targeted cells," Sci. Robot., vol. 3, no. 19, pp. 1–12, 2018.
[27] E. Diller and M. Sitti, "Three-dimensional programmable assembly by untethered magnetic robotic micro-grippers," Adv. Funct. Mater., vol. 24, no. 28, pp. 4397–4404, 2014.
[28] F. Ongaro et al., "Autonomous planning and control of soft untethered grippers in unstructured environments," J. Micro-Bio Robot., vol. 12, no. 1¨C4, pp. 45–52, 2017.
[29] S. Tottori et al., "Magnetic helical micromachines: Fabrication, controlled swimming, and cargo transport," Adv. Mater., vol. 24, no. 6, pp. 811–816, 2012.